On the dust geometry in radio-loud active galactic nuclei

Hermine Landt[1]⋆, Catherine L. Buchanan[1] and P. Barmby[2]

[1]*School of Physics, University of Melbourne, Parkville, VIC 3010, Australia*
[2]*Department of Physics and Astronomy, University of Western Ontario, 1151 Richmond Street, London, ON N6A 3K7, Canada*

ABSTRACT

We use photometric and spectroscopic infrared observations obtained with the *Spitzer Space Telescope* of 12 radio-loud active galactic nuclei (AGN) to investigate the dust geometry. Our approach is to look at the change of the infrared spectral energy distribution (SED) and the strength of the 10 μm silicate feature with jet viewing angle. We find that (i) a combination of three or four blackbodies fits well the infrared SED; (ii) the sources viewed closer to the jet axis appear to have stronger warm ($\sim 300 - 800$ K) and cold ($\sim 150 - 250$ K) dust emissions relative to the hot component; and (iii) the silicate features are always in emission and strongly redshifted. We test clumpy torus models and find that (i) they approximate well the mid-infrared part of the SED, but significantly underpredict the fluxes at both near- and far-infrared wavelengths; (ii) they can constrain the dust composition (in our case to that of the standard interstellar medium); (iii) they require relatively large ($\sim 10\% - 20\%$ the speed of light) redward displacements; and (iv) they give robust total mass estimates, but are insensitive to the assumed geometry.

Key words: galaxies: active – galaxies: nuclei – infrared: galaxies – quasars: general

1 INTRODUCTION

Some active galactic nuclei (AGN) exhibit in their optical spectra both broad ($\sim 1\% - 5\%$ the speed of light) and narrow emission lines (type 1 AGN) and some only narrow (type 2 AGN). The existence of apparently two distinct classes of AGN has been explained within unified schemes by orientation effects: an optically thick, dusty torus (or warped disc) located outside the accretion disc obscures the broad emission line region for some lines of sight (see reviews by Lawrence 1987; Antonucci 1993; Urry & Padovani 1995). The strongest observational evidence interpreted in favour of such a torus are broad emission lines in the polarized, scattered light of numerous type 2 AGN (e.g., Antonucci & Miller 1985; Cohen et al. 1999; Lumsden et al. 2001) and significant infrared emission in the continuua of most AGN. However, details of the physical state of this torus, its precise geometry and location remain unconstrained to this day.

The putative torus will absorb a significant fraction of the nuclear (accretion) luminosity and reradiate it strongly in the infrared. The dust radiative transfer problem was first investigated for a toroidal geometry by Krolik & Begelman (1988) and Pier & Krolik (1992, 1993). Because of the difficulties in modelling a clumpy medium they assumed a uniform density distribution, although they noted that the dust must be concentrated in clouds to protect the grains. Their models reproduced the gross features of the observed spectral energy distributions (SEDs), but some major problems remained: (i) the torus was predicted to emit anisotropically; (ii) the generated emission at far-infrared wavelengths was insufficient; (iii) early observations of type 1 AGN did not show the predicted strong 10 μm silicate emission features (Roche et al. 1991; Clavel et al. 2000; Spoon et al. 2002); and (iv) the required geometrical thickness was difficult to support (Krolik 2007; Shi & Krolik 2008). These problems persisted in all the following studies, which also employed continuous density distributions (e.g., Granato & Danese 1994; Efstathiou & Rowan-Robinson 1995; van Bemmel & Dullemond 2003).

More recently, Nenkova et al. (2002, 2008a,b) have developed a formalism for handling radiative transfer in clumpy media and have applied it to AGN. Their model is able to reproduce some of the observed SED features, if a small number of clouds along equatorial rays is assumed. In particular, the infrared SEDs and strengths of the silicate emission features are now predicted to be largely independent of orientation and a large range of temperatures can coexist at a given distance from the central source, as required by new interferometric results (Tristram et al. 2007, 2009). Nevertheless, the situation is far from being resolved. Observations with the *Spitzer Space Telescope* have

⋆ E-mail: hlandt@unimelb.edu.au

now started to show strong silicate emission features in quasars and absorption troughs in sources viewed edge-on, just as predicted by Pier & Krolik (e.g., Siebenmorgen et al. 2005; Haas et al. 2005; Hao et al. 2005; Weedman et al. 2005; Buchanan et al. 2006; Shi et al. 2006; Ogle et al. 2006; Cleary et al. 2007; Hao et al. 2007; Schweitzer et al. 2008; Thompson et al. 2009; Hiner et al. 2009).

Unravelling the structure of the dust obscuration is essential to our understanding of AGN. In this paper we use for the first time both photometric and spectroscopic *Spitzer Space Telescope* observations of radio-loud AGN, for which actual viewing angles can be determined, to investigate this topic. In Section 2 we introduce the sample and discuss the method used to derive viewing angles. The infrared data are presented in Section 3, whereas in Section 4 we confront theory with observations. Finally, in Section 5 we conclude and summarize our main results.

Throughout this paper we have assumed cosmological parameters $H_0 = 70$ km s^{-1} Mpc^{-1}, $\Omega_M = 0.3$, and $\Omega_\Lambda = 0.7$.

2   THE SAMPLE

The presence of strong radio jets in radio-loud AGN gives us a unique opportunity to derive actual viewing angles, θ (defined as the angle between the jet and the observer's line of sight), for this object class. Following Ghisellini et al. (1993), we use here the method that combines apparent jet speeds, β_a (in units of the speed of light), with relativistic Doppler factors, δ, to calculate viewing angles.

If β_a is available from proper motion measurements and δ can be separately estimated, then the viewing angle is:

$$\tan\theta = \frac{2\beta_a}{\beta_a{}^2 + \delta^2 - 1}. \tag{1}$$

The largest uncertainty of this approach lies with the determination of δ, which involves several observables. Using the classical condition that the (predicted) synchrotron self-Compton (SSC) flux should not exceed the observed high-energy flux, δ can be calculated as (Marscher 1987):

$$\delta = f(\alpha)F_m \left[\frac{\ln(\nu_b/\nu_m)}{F_x \Theta_d^{6+4\alpha} \nu_x^\alpha \nu_m^{5+3\alpha}} \right]^{1/(4+2\alpha)} (1+z), \tag{2}$$

where α is the spectral index of the thin synchrotron emission (assumed to be 0.75), ν_b is the synchrotron high-frequency cut-off (assumed to be 10^{14} Hz), the function $f(\alpha) \simeq 0.08\alpha + 0.14$ (assumed to be 0.2), and the redshift z is known. The synchrotron flux F_m (in Jy) at the self-absorption frequency ν_m (in Hz) of the core component with angular size Θ_d (in mas) need to be determined from appropriate Very Large Baseline Interferometry (VLBI) observations. Observables are also the high-frequency (X-ray) flux F_x (in Jy) at the (X-ray) frequency ν_x (in keV) of this component.

The most critical parameters in eq. (2) are the VLBI observables ν_m and Θ_d, and these are in general difficult and expensive to determine. The determination of ν_m ideally requires a VLBI spectrum (i.e., high spatial resolution observations at different radio frequencies) of the strongest (core) component or a sophisticated spectral decomposition of a low-resolution spectrum to isolate the different (VLBI)

components. On the other hand, observationally Θ_d will depend on the frequency itself (the higher the frequency, the higher the spatial resolution) and, therefore, will be an upper limit only. This then makes δ strictly speaking a lower limit and so the viewing angle an upper limit.

As Ghisellini et al. (1993) (and also Rokaki et al. 2003) have shown, this method samples a wide range of viewing angles, including the regime of $20° < \theta < 60°$ that we are interested in. Vermeulen & Cohen (1994) presented a large compilation of sources with measured jet proper motions. We have updated their list with later literature and have calculated viewing angles for all the sources. From the updated list, and restricting ourselves to $z \lesssim 1$ in order to keep the emitted far-infrared accessible, we have chosen for observations with the *Spitzer Space Telescope* all sources with viewing angles $\theta \gtrsim 20°$ (12 objects; see Table 1). We note that the source 3C 207 no longer obeys this criterion based on most recent proper motion data, but is kept in the sample for comparison. The cut in viewing angle avoids sources with infrared emission dominated by the relativistically beamed jet, so allowing for a reliable determination of the dust SED. All selected sources are radio quasars (i.e., type 1 AGN), except for 3C 84 (= NGC 1275), which is a radio galaxy (i.e., type 2 AGN).

The total errors in our viewing angles are difficult to determine, since the errors in the Doppler factors δ are largely unconstrained. But, given the errors in the proper motions (Table 1, column (8)), we derive an average lower limit on them of $\sim 50\%$. In this respect, we note that Rokaki et al. (2003) argue that it is unlikely that Doppler factors estimated using eq. (2) are wrong by a very large factor, since they observe excellent correlations between δ and several emission line properties. We concur with this conclusion given our results in Section 4.1.1. In addition, a consistency check that we carry out in Section 4.1.3 supports the notion that the trend in viewing angle that we obtain for our sample is qualitatively correct.

3   OBSERVATIONS AND DATA REDUCTION

We observed our sample with the *Spitzer Space Telescope* in Cycle 1 (ID: 3551). We used all its instruments and imaged the sources with the Infrared Array Camera (IRAC; Fazio et al. 2004) in four bands (3.6, 4.5, 5.8, and 8.0 μm) and with the Multiband Imaging Photometer for Spitzer (MIPS; Rieke et al. 2004) in three bands (24, 70, and 160 μm). In addition we obtained low-resolution spectroscopy with the Infrared Spectrograph (IRS; Houck et al. 2004) in staring mode using the appropriate short and long order modules in order to cover well the rest-frame wavelength region around 10 μm.

In Tables 2 and 3 we list the details for the photometric and spectroscopic observations, respectively. Some of the approved observations were allocated to other programs and were accessible to us only after the proprietary period expired. We also note that we now include in this study all low-resolution (staring mode) IRS spectra available in the archive for our sources and not only those initially requested. In the following we describe the data reduction process and measurements.

Table 1. General Properties of the Sample

Object Name	IAU Name	R.A.(J2000)	Decl.(J2000)	z	θ [deg]	$\mu_{\rm r}$ [mas/yr]	$\sigma_{\mu_{\rm r}}$ [mas/yr]	Ref.	β_a	$\nu_{\rm m}$ [GHz]	$F_{\rm m}$ [Jy]	$\Theta_{\rm d}$ [mas]	Ref.	$F_{\rm x}$ [μJy]	Ref.	δ
(1)	(2)	(3)	(4)	(5)	(6)	(7)	(8)	(9)	(10)	(11)	(12)	(13)	(14)	(15)	(16)	(17)
III Zw 2[*]	0007+106	00 10 31.0	+10 58 30	0.090	28	0.166	0.016	MOJAVE	0.99	15	0.79	0.15	B05	1.101	Pic05	1.9
3C 47	0133+207	01 36 24.4	+20 57 27	0.425	18	0.24	0.05	VC94	6.21	8	0.07	0.20	H02	0.363	Ha06	0.4
3C 84	0316+413	03 19 48.1	+41 30 42	0.018	31	0.266	0.050	MOJAVE	0.32	28	6.50	0.35	R83	2.400	E06	1.4
S5 0615+820	0615+820	06 26 03.0	+82 02 26	0.710	49	0.053	0.020	MOJAVE	2.12	2	0.86	3.50	F00	0.040	S97	0.4
3C 207	0838+133	08 40 47.6	+13 12 24	0.681	8	0.334	0.030	MOJAVE	12.94	8	0.60	0.28	H02	0.120	G03	3.0
3C 245	1040+123	10 42 44.6	+12 03 31	1.029	18	0.11	0.05	VC94	5.87	11	0.59	0.33	H87	0.160	G03	1.7
3C 263	1137+660	11 39 57.0	+65 47 49	0.646	48	0.06	0.02	VC94	2.23	8	0.12	0.37	H02	0.290	Ha02	0.3
3C 334	1618+177	16 20 21.8	+17 36 24	0.555	34	0.10	0.03	VC94	3.27	11	0.09	0.20	H92	0.342	Ha99	0.4
3C 336	1622+238	16 24 39.1	+23 45 12	0.927	23	0.10	0.07	H02	4.94	8	0.01	0.20	H02	3.700	P96	0.1
4C +34.47	1721+343	17 23 20.8	+34 17 58	0.206	30	0.28	0.03	VC94	3.72	11	0.11	0.24	Ho92a	1.467	Pa04	0.2
4C +28.45	1830+285	18 32 50.2	+28 33 36	0.594	24	0.13	0.04	VC94	4.50	5	0.50	0.30	Ho92b	0.309	B97	0.8
3C 390.3	1845+797	18 42 09.0	+79 46 17	0.056	48	0.605	0.010	MOJAVE	2.26	11	0.41	0.59	L81	7.600	E06	0.1

The columns are: (1) object name; (2) IAU name; (3) and (4) position, and (5) redshift from the NASA/IPAC Extragalactic Database (NED); (6) jet viewing angle calculated with the synchrotron self-Compton (SSC) formalism using the following observables: (7) proper motion and (8) 1σ error on proper motion, taken from reference in (9), where MOJAVE: large project for 'Monitoring Of Jets in AGN with VLBA Experiments' (e.g., Kellermann et al. 2004; Lister et al. 2009), VC94: Vermeulen & Cohen (1994), and H02: Hough et al. (2002); (10) apparent jet speed calculated from column (7); (11) synchrotron self-absorption frequency; (12) flux and (13) size at (11) of the core component; (14) reference for columns (11)-(13), where B05: Brunthaler et al. (2005), F00: Fey & Charlot (2000), H87: Hough & Readhead (1987), H92: Hough et al. (1992), H02: Hough et al. (2002), Ho92a: Hooimeyer et al. (1992a), Ho92b: Hooimeyer et al. (1992b), L81: Linfield (1981), R83: Readhead et al. (1983); (15) X-ray flux at 1 keV, taken from the reference in (16), where B97: Brinkmann et al. (1997), E06: Evans et al. (2006), G03: Gambill et al. (2003), Ha99: Hardcastle & Worrall (1999), Ha02: Hardcastle et al. (2002), Ha06: Hardcastle et al. (2006), P96: Prieto (1996), Pa04: Page et al. (2004), Pic05: Piconcelli et al. (2005), S97: Sambruna (1997); and (17) relativistic Doppler factor calculated from columns (11)-(13) and (15).

[*] position of the northern most source in a galaxy triplet

Table 2. *Spitzer* Photometry Journal of Observations

Object Name	ID	IRAC observation date	texp. [sec]	ID	24 μm observation date	texp. [sec]	ID	MIPS 70 μm observation date	texp. [sec]	ID	160 μm observation date	texp. [sec]
(1)	(2)	(3)	(4)	(5)	(6)	(7)	(8)	(9)	(10)	(11)	(12)	(13)
III Zw 2	3551	2004 Dec 15	4× 2	86	2004 Dec 26	2× 3	86	2004 Dec 26	2× 3	3551	2005 Aug 2	10×10
3C 47	3551	2005 Jan 16	4× 2	3551	2005 Jan 29	3× 3	3551	2005 Jan 29	3×10	3551	2005 Jan 29	10×10
3C 84	3228	2005 Feb 20	5×30	3551	2005 Feb 26	3× 3	3551	2005 Feb 26	3× 3	3418	2005 Feb 1	5×10
S5 0615+820	3551	2004 Nov 20	4×12	3551	2005 Mar 3	3× 3	3551	2005 Mar 3	3×10	3551	2005 Mar 3	10×10
3C 207	3551	2005 May 10	4×12	74	2005 Apr 10	1×10	74	2005 Apr 10	4×10	74	2005 Apr 10	4×10
3C 245	40072	2008 Jun 10	1×30	40072	2008 Jan 6	1×10						
3C 263	3551	2004 Nov 1	4× 2	74	2005 Apr 9	1× 3	74	2005 Apr 9	1×10	74	2005 Apr 9	4× 3
3C 334	3551	2005 Mar 26	4× 2	74	2005 Apr 7	1×10	74	2005 Apr 7	1×10	74	2005 Apr 7	4×10
3C 336	3551	2005 Mar 27	4×12	74	2005 Apr 12	1×10	74	2005 Apr 12	6×10	74	2005 Apr 12	4×10
4C +34.47	3551	2005 Mar 30	4× 2	3551	2005 Apr 6	3× 3	3551	2005 Apr 6	3×10	3551	2005 Apr 6	10×10
4C +28.45	3551	2004 Oct 8	4× 2	3551	2004 Oct 17	3× 3	3551	2004 Oct 17	3×10	3551	2004 Oct 17	10×10
3C 390.3	50763	2008 May 13	9×12	3327	2004 Oct 17	4×10	3551	2004 Oct 18	3×10	3551	2004 Oct 18	10×10

The columns are: (1) object name; for photometry with the Infrared Array Camera (IRAC) (2) program number, (3) observation date and (4) exposure time; for photometry with the Multiband Imaging Photometer for Spitzer (MIPS) (5) program number, (6) observation date, and (7) exposure time in the 24 μm band, (8) program number, (9) observation date, and (10) exposure time in the 70 μm band, and (11) program number, (12) observation date, and (13) exposure time in the 160 μm band.

3.1   The photometry

The IRAC data were processed with the *Spitzer* Science Center (SSC) pipeline v14.0, except for 3C 84 and 3C 390.3, for which we used the pipeline v18.7.0 since it corrects artifacts near bright sources. We measured flux densities from 3.6 to 8.0 μm on the 'post-basic calibrated data (BCD)' mosaics produced by the pipeline. For 3C 84 and 3C 390.3, mosaics made from the short-exposure images taken in high-dynamic range mode were used. We used aperture photometry and adopted a 10-pixel (12 arcsec) source radius, with background counts estimated in a 10-20 pixel (12-24 arcsec) radius annulus and subtracted. The sources 3C 336 and S5 0615+820 had other objects nearby, therefore, we measured their fluxes in smaller 5-pixel (6 arcsec) apertures.

We note that the 3.6 and 4.5 μm images of III Zw 2 show that this object may be a blend of two very close sources, and so flux densities at these wavelengths could be overestimated. The 3.6 and 4.5 μm images of 3C 84 probably are contaminated by an extended component since no separate central point source is visible. For the source 3C 390.3 two data sets were available separated by about four years and we have considered both. However, the observations contemporaneous with the MIPS photometry and IRS spectroscopy were severely affected by saturation, and, therefore, not useful for our purpose.

All IRAC flux densities were aperture-corrected using the values in the IRAC Data Handbook (v3.0, 2006). No 'array-location-dependent' photometric correction was applied, since these are red sources and do not require such a correction. Table 4 lists our results. All sources have been detected in all four IRAC bands. We give 1σ uncertainties estimated using the standard IRAF photometry formula. We note that these values do not include the error in absolute calibration (a few per cent; Reach et al. 2005).

The MIPS data were reprocessed with the SSC pipeline v16.1.0. Measurements on 24 μm images followed standard procedures using the post-BCD pipeline mosaics. We mea-

sured flux densities in the standard aperture (35″ radius) with the recommended aperture correction of 1.082 applied, except in the case of 3C 336 where a 7″ radius aperture with a correction factor of 1.61 were used. The flux density measured for 3C 84 (2.9 Jy) is formally above the saturation limit for 3-sec. exposures, but the object is only 'soft-saturated' and the pipeline correctly replaced the saturated pixels with values from the 0.5-sec. exposures taken as part of the photometry AOR. Table 4 lists the results. All sources have been detected. We have computed uncertainties using the same method as for IRAC, which again do not include the errors in the absolute calibration ($\sim 2\%$; Engelbracht et al. 2007).

For the measurements at 70 μm we used mostly the pipeline-produced 'filtered' mosaics, although in a few cases we remade the mosaics using time- and column-filtering of the BCDs to remove negative sidelobes around bright sources. Per the MIPS Data Handbook (v3.3.1) we measured the flux densities in 35″ radius apertures with sky annuli of 39-60 arcsec and an aperture correction of 1.22. Our results are listed in Table 4. Following Carpenter et al. (2008), we calculated uncertainties in the flux density using a similar equation to that for IRAC and MIPS-24, but neglecting Poisson noise and applying instead multiplicative factors to account for the noise correlation between pixels due to resampling during mosaicing and excess sky noise due to the data-taking procedure. The absolute calibration uncertainty at 70 μm is 5% (Gordon et al. 2007), again not included in the tabulated values. The source 3C 84 is very bright at 70 μm but, as at 24 μm, is just below the saturation limit. Five sources were not detected at 70 μm and we give only 3σ upper limits. One source (3C 245) did not have MIPS-70 data.

For the measurements at 160 μm we used the pipeline-produced 'filtered' BCDs and made mosaics using the MOPEX software (Makovoz & Marleau 2005). However, for the bright source 3C 84 and the source 3C 390.3 that has

another bright object nearby we produced mosaics from the unfiltered images. Following the MIPS Data Handbook, we measured flux densities in $48''$ apertures with sky annuli of 64-128 arcsec and an aperture correction of 1.60. The only exception was the source 3C 390.3. Due to the presence of a nearby brighter source separated by ~ 1 arcmin, we measured its flux density instead in an aperture of 32" with an aperture correction of 1.97. Our results are listed in Table 4. Uncertainties for all sources were calculated as described above for the MIPS-70 data. The absolute calibration uncertainty at 160 μm is 12% (Stansberry et al. 2007) and is not included in the tabulated values. The source 3C 84 is very bright at 160 μm and at the saturation limit, therefore, its flux density is highly uncertain and is taken to be 20% (Stansberry et al. 2007). Seven sources were not detected at 160 μm and we give only 3σ upper limits. One source (3C 245) did not have MIPS-160 data.

The archival MIPS data we used for four objects, namely, 3C 207, 3C 263, 3C 334 and 3C 336, were analysed also by Cleary et al. (2007). Our flux densities in the 24 μm , 70 μm and 160 μm bands are consistent with theirs within 2σ, however, contrary to these authors we regard the sources 3C 207 and 3C 263 as undetected in the MIPS-70 images and the sources 3C 334 and 3C 336 as detected in the MIPS-160 images.

3.2   The spectroscopy

The raw data were processed through the SSC pipeline v15.3 for the short-low (SL) modules and v17.2 for the long-low (LL) modules. The BCDs produced by the pipeline were cleaned for rogue pixels using the IRSCLEAN software[1], then spectra were extracted using the SMART software (Higdon et al. 2004). Where multiple exposures were obtained, the two-dimensional spectral images were median-combined.

Two positions (nods) were observed for each target, and sky subtraction was performed on the images, by subtracting the off-source nod position image from the on-source image for each module. Spectra were extracted and the fluxes calibrated using the default tapered column apertures for each module. The modules at each nod position were merged and the edges and overlapping regions trimmed. The spectra from the two nod positions were then averaged to produce the final spectrum. Uncertainty images provided by the pipeline and propagated through SMART were used to produce the uncertainties on the final spectra. Our results are shown in Fig. 1.

4   THE DUST GEOMETRY

Fig. 1 shows the infrared SEDs for our sources plotted to have the same dynamic range. In the near-infrared we have supplemented the *Spitzer* data with ground-based photometry in the J, H and K_s bands from the Two Micron All-Sky Survey (2MASS; Skrutskie et al. 2006). All sources but one

are included in the Point Source Catalogue of this survey and we list the flux densities in Table 5. For the undetected source S5 0615+820 we have derived 3σ upper limits based on the image plate specifications.

4.1   General trends

Before testing detailed theoretical models with our data (Section 4.2) we want to first quantify the observations, with particular emphasis on revealing trends that any acceptable model will have to account for.

4.1.1   The shape and width of the SED

In the simplest approach we can approximate our observations with a set of blackbodies. For this purpose we have fitted our data with the C routine MPFIT (version 1.1; Markwardt 2009), which uses the Levenberg-Marquardt technique to solve the least-squares problem. We have tried several numbers of blackbodies and have found that three or four components were required to obtain an acceptable fit. We have fitted for the temperatures and flux scalings of the individual blackbody components, meaning that our fits have either six or eight free parameters. Our results are listed in Table 6 and shown in Fig. 1, where dotted black curves indicate the individual components and the solid black curve their sum.

We have included in the fit only the continuum part of the IRS spectrum, i.e., we have excluded strong narrow emission lines and the silicate emission features, and we have rebinned it to $\Delta \log \lambda = 0.05$ μm in order to ensure a similar weighting between spectroscopy and photometry. However, in the case of the source 3C 245, for which neither MIPS-70 nor MIPS-160 data were available, we have left the spectrum unbinned. We have treated all photometry upper limits as detections and have assumed their 1σ values as the error. We have not considered the 2MASS photometric data points, since not only they appear to sample a different component (most likely the onset of the accretion disc) but they were obtained several years before our *Spitzer* observations. The two exceptions were III Zw 2 and 4C +34.47, for which we included the 2MASS K_s point, since it connected smoothly to the IRAC photometry and thus presented an important constraint on the hottest blackbody component. The IRAC data we use for the source 3C 390.3 was taken four years after the MIPS and IRS observations and variability by a factor of ~ 1.5 is observed. Therefore, assuming that variability does not change the spectral slope, we have scaled these data to the IRS spectrum before including them in the fit.

Our sample is evenly split into sources best-fit by three and four blackbodies. For the source 3C 245, the far-infrared part of the SED is not constrained and, therefore, we cannot exclude that four instead of three blackbodies might be required. In all sources but two the resulting fit is 'good' in a statistical sense (χ^2_ν of a few). In the two brightest sources (3C 84 and 3C 390.3) the resulting fit appears good to the eye and the large χ^2_ν-values could be mainly due to the much smaller relative measurement errors involved. Resulting temperatures for the hot, warm, cold and cool blackbody components are in the ranges $T_{\rm hot} \sim 1200 - 2000$

---

[1] IRSCLEAN was written by the IRS GTO team (G. Sloan, D. Devost, & B. Sargent). It is distributed by the *Spitzer* Science Center at Caltech.

Table 3. *Spitzer* Spectroscopy Journal of Observations

Object Name	ID	observation date	peak-up	SL2 texp. [sec]	SL1 texp. [sec]	ID	observation date	peak-up	LL2 texp. [sec]	LL1 texp. [sec]
(1)	(2)	(3)	(4)	(5)	(6)	(7)	(8)	(9)	(10)	(11)
III Zw 2	86	2005 Jul 10	blue	4× 30	2× 60					
3C 47	3551	2005 Jan 11	none	–	4× 14	3551	2005 Jan 11	none	4×120	–
3C 84	14	2004 Aug 30	blue	2× 14	2× 14	14	2004 Aug 30	blue	4× 6	4× 6
S5 0615+820	3551	2004 Oct 23	none	–	4× 60	3551	2004 Oct 23	none	4×120	–
3C 207	3551	2004 Apr 15	none	–	4× 60	74	2005 Nov 15	blue	4×120	4×120
3C 245						40314	2008 Jan 10	none	–	12×120
3C 263	3551	2004 Nov 16	none	–	4× 60	74	2004 Apr 14	blue	4×120	4×120
3C 334	3551	2005 Mar 14	none	–	4× 14	74	2004 Jul 16	blue	4×120	4×120
3C 336						74	2004 Mar 22	blue	4×120	4×120
4C +34.47	3551	2005 Mar 14	none	–	4× 6	3551	2005 Mar 14	none	4× 14	–
4C +28.45	3551	2004 Oct 23	none	–	4× 60	3551	2004 Oct 23	none	4×120	–
3C 390.3	82	2004 Mar 24	blue	1×240	1×240	82	2004 Mar 24	blue	4×120	4×120

The columns are: (1) object name; for low-resolution spectroscopy with the Infrared Spectrograph (IRS) short order modules (2) program number, (3) observation date, (4) peak-up imaging array and exposure times for the slits (5) SL2 (5.2-8.7 μm) and (6) SL1 (7.4-14.5 μm); for low-resolution spectroscopy with the IRS long order modules (7) program number, (8) observation date, (9) peak-up imaging array and exposure times for the slits (10) LL2 (14.0-21.3 μm), and (11) LL1 (19.5-38.0 μm).

Table 4. *Spitzer* Photometry Results

Object Name	$F_{3.6}$ [mJy]	$\sigma_{3.6}$ [mJy]	$F_{4.5}$ [mJy]	$\sigma_{4.5}$ [mJy]	$F_{5.8}$ [mJy]	$\sigma_{5.8}$ [mJy]	$F_{8.0}$ [mJy]	$\sigma_{8.0}$ [mJy]	F_{24} [mJy]	σ_{24} [mJy]	F_{70} [mJy]	σ_{70} [mJy]	F_{160} [mJy]	σ_{160} [mJy]
III Zw 2	22.2	0.1	28.1	0.1	35.3	0.4	48.8	0.2	138	1	128	17	59	6
3C 47	5.3	0.1	6.9	0.1	9.2	0.3	11.2	0.2	36.8	0.4	37	10	<27	
3C 84	75.81	0.09	89.12	0.06	132.2	0.2	291.1	0.2	2930	3	3990	33	4350	870
S5 0615+820	0.63	0.01	0.78	0.01	1.00	0.05	1.24	0.02	4.8	0.3	<18		<21	
3C 207	1.54	0.01	2.09	0.02	2.75	0.07	3.94	0.07	13.2	0.4	<26		<36	
3C 245	1.54	0.01	2.12	0.01	3.66	0.03	5.55	0.03	20.9	0.6				
3C 263	5.5	0.1	7.3	0.1	8.9	0.3	11.5	0.2	26.7	0.7	<35		<18	
3C 334	3.44	0.09	4.7	0.1	5.5	0.3	7.4	0.2	36.0	0.3	83	11	28	7
3C 336	0.76	0.01	1.04	0.01	1.44	0.03	1.93	0.03	3.9	0.1	19	5	62	10
4C +34.47	9.0	0.1	11.9	0.1	13.8	0.3	18.2	0.2	59.9	0.5	<21		<15	
4C +28.45	2.19	0.09	3.4	0.1	3.8	0.3	5.4	0.2	18.2	0.4	<24		<33	
3C 390.3	56.0	0.1	66.2	0.1	73.1	0.2	89.0	0.2	234.0	0.2	120	6	<24	

Table 5. Two Micron All-Sky Survey (2MASS) Fluxes

| Object Name	J (1.235 μm) [mJy]	σ_J [mJy]	H (1.622 μm) [mJy]	σ_H [mJy]	K_s (2.159 μm) [mJy]	σ_{K_s} [mJy]
III Zw 2	4.5	0.2	6.3	0.3	12.9	0.3
3C 47	0.46	0.05	0.68	0.07	1.01	0.09
3C 84	12.4	0.9	16.6	1.2	20	1
S5 0615+820	<0.13		<0.22		<0.26	
3C 207	0.34	0.05	0.42	0.06	0.64	0.07
3C 245	0.40	0.05	0.41	0.08	0.51	0.08
3C 263	1.87	0.07	1.79	0.08	2.30	0.09
3C 334	0.96	0.05	1.10	0.08	1.54	0.08
3C 336	0.40	0.04	0.33	0.07	0.45	0.08
4C +34.47	2.72	0.06	3.03	0.09	4.7	0.1
4C +28.45	0.32	0.05	0.53	0.07	0.73	0.06
3C 390.3	5.8	0.2	9.4	0.3	13.7	0.4
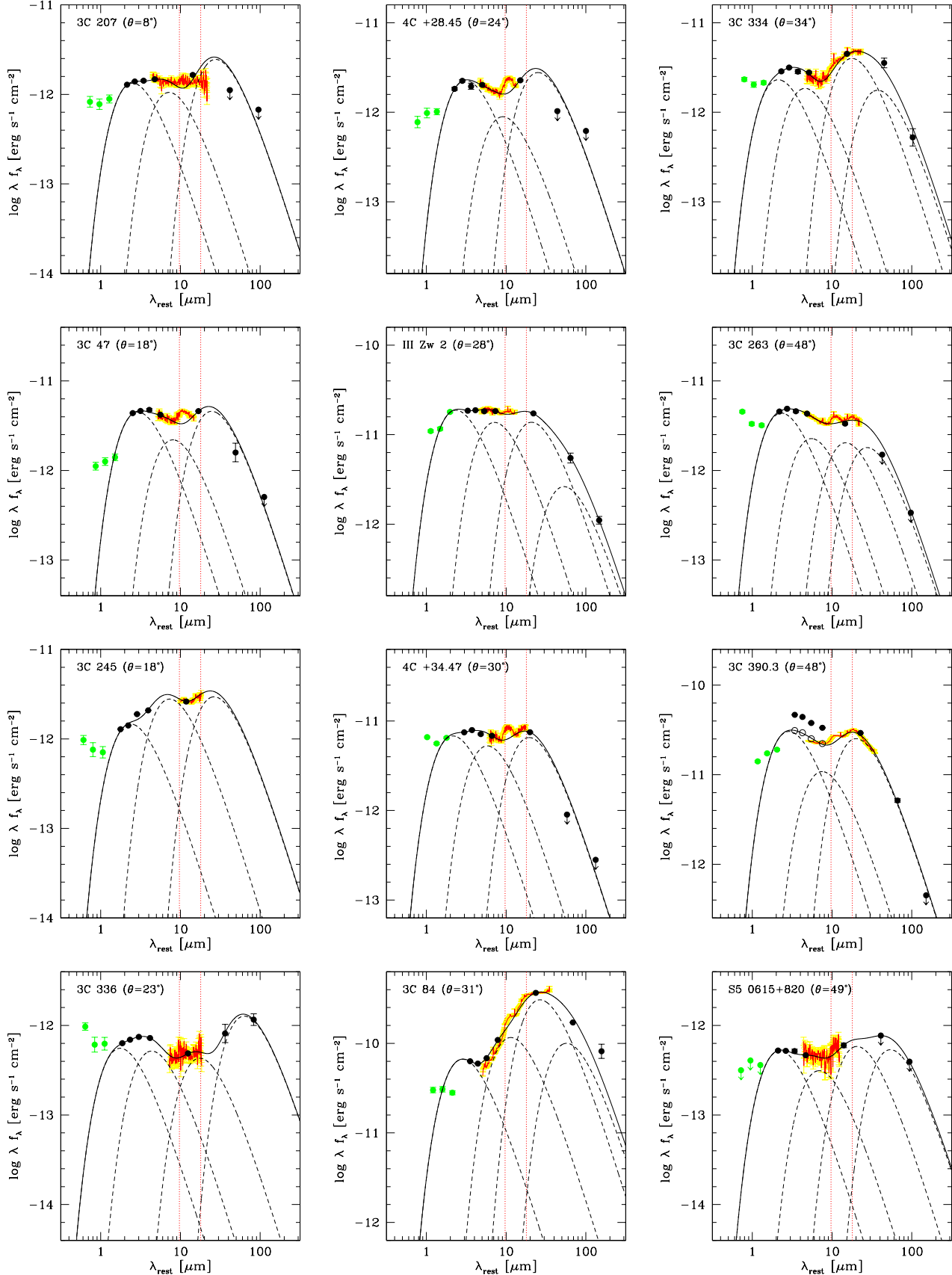
Figure 1. Infrared spectral energy distributions plotted as rest-frame wavelength versus observed integrated flux. Filled black and green circles indicate *Spitzer* IRAC and MIPS and 2MASS photometry, respectively. The *Spitzer* IRS spectrum is shown in red, with its errors in yellow and the locations of the silicate features marked (red dotted lines). The dotted and solid black curves show the best-fit blackbodies and their sum, respectively. The fit for the source 3C 390.3 included the IRAC data scaled to the IRS spectrum (open black circles).

Table 6. Blackbody Fit Results

Object Name[*]	θ [deg]	T_{hot} [K]	T_{warm} [K]	T_{cool} [K]	T_{cold} [K]	f_{hot} [erg/s/cm^2]	f_{warm} [erg/s/cm^2]	f_{cool} [erg/s/cm^2]	f_{cold} [erg/s/cm^2]	χ^2_ν/dof
(1)	(2)	(3)	(4)	(5)	(6)	(7)	(8)	(9)	(10)	(11)
3C 207	8	1459	509	133	–	1.33e−12	1.05e−12	2.46e−12	–	5.3/8
3C 47	18	1251	456	149	–	4.48e−12	2.20e−12	4.58e−12	–	1.62/7
3C 245	18	1543	501	139	–	1.47e−12	2.78e−12	2.95e−12	–	8.1/98
3C 336	23	2087	842	210	58	5.56e−13	5.17e−13	4.31e−13	1.27e−12	1.27/4
4C +28.45	24	1175	403	146	–	2.27e−12	8.92e−13	2.78e−12	–	1.99/7
III Zw 2	28	1561	514	176	69	1.87e−11	1.37e−11	1.37e−11	2.63e−12	3.8/7
4C +34.47	30	1702	632	189	–	6.80e−12	5.27e−12	6.53e−12	–	4.2/7
3C 84	31	1290	321	138	64	6.65e−11	1.16e−10	3.07e−10	1.00e−10	1491/8
3C 334	34	1733	799	207	98	2.31e−12	1.85e−12	4.00e−12	1.76e−12	3.7/7
3C 263	48	1581	666	247	133	4.37e−12	2.27e−12	2.04e−12	1.80e−12	1.42/7
3C 390.3[†]	48	1274	488	183	–	3.04e−11	1.08e−11	2.53e−11	–	757/11
S5 0615+820	49	1654	533	179	68	5.22e−13	3.13e−13	5.83e−13	5.36e−13	0.55/6

The columns are: (1) object name; (2) jet inclination angle; temperature of the (3) hot, (4) warm, (5) cool, and (6) cold blackbody component; peak flux of the (7) hot, (8) warm, (9) cool, and (10) cold blackbody component; and (11) reduced χ^2 value and number of degrees of freedom.

[*] objects presented in order of increasing jet viewing angle

[†] fit performed to the IRAC data scaled to the IRS spectrum
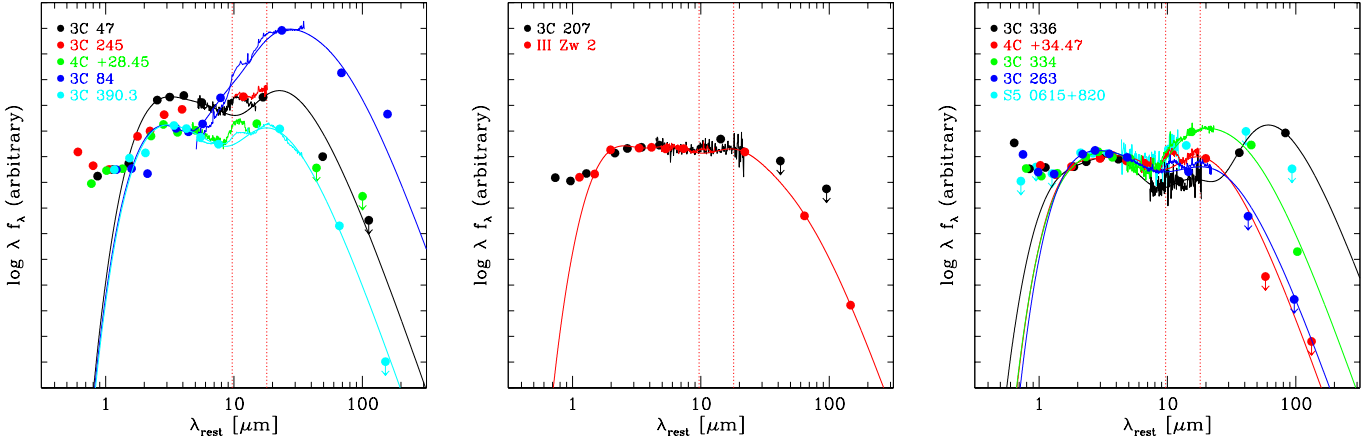
Figure 2. Infrared spectral energy distributions from Fig. 1 normalized at $\sim 1\ \mu$m, grouped by the relative strength of the hot blackbody component and shown from left to right in decreasing order. The solid line indicates the sum of the best-fit blackbodies and has been omitted for the sources 3C 207, 3C 245, 4C +28.45, and S5 0615+820, for which the long-wavelength end is not well constrained. The locations of the silicate features are marked by the red dotted lines.

K, $T_{\text{warm}} \sim 300 - 800$ K, $T_{\text{cool}} \sim 150 - 250$ K, and $T_{\text{cold}} \sim 60 - 150$ K, respectively. Note that the hottest blackbody component reaches values that are typical of the dust sublimation temperature for most grain compositions ($\approx 1000 - 2000$ K; Salpeter 1977).

Three important trends are revealed by this simplistic approach. Firstly, the strengths of the individual blackbodies relative to each other vary substantially between sources, giving the impression that they indeed sample discrete components of a certain temperature rather than a single component with a smooth temperature distribution. Secondly, the cool (~ 200 K) blackbody component is prominent in all sources and appears roughly as strong or stronger than the hot blackbody component. Only in the source 3C 263 is this behaviour reversed. And thirdly, the warm (~ 500 K) blackbody component is often weak, thus introducing a

sharp 'dip' in the SED just blueward of the 10 μm silicate feature. We also note that, although in most cases we did not include the 2MASS K_s point in the fit, it is often approximated well by the hot blackbody component.

In order to investigate if orientation determines to some degree the relative strengths of the individual blackbody components in a given source, we have normalized the SEDs at $\sim 1\ \mu$m and have grouped them in order of the relative strength of the hot blackbody component. In Fig. 2 we show our sources in three distinct groups with the average relative strength of the hot blackbody component decreasing from left to right. This representation of the SEDs suggests two important results. Firstly, no trend with orientation seems to be present for the hot dust. In particular, although the two sources with the strongest hot blackbody components (3C 47 and 3C 245) are among those with the smallest esti-
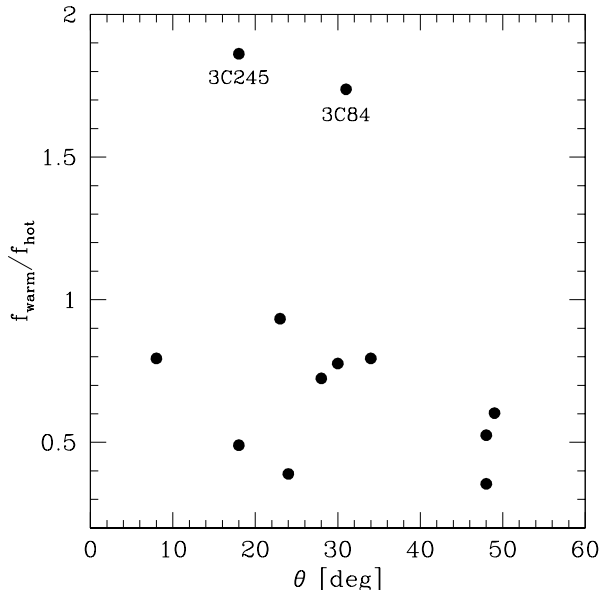
Figure 3. The ratio between the peak fluxes of the warm and hot blackbody components versus the jet viewing angle.
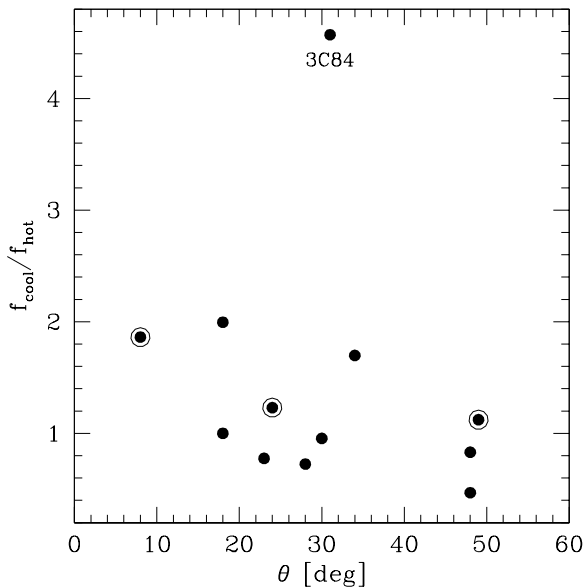

Figure 4. Same as Fig. 3 for the cool blackbody component. This component is likely to be overestimated for three sources (3C 207, 4C +28.45, and S5 0615+820; encircled points).

mated viewing angles, the main prediction of torus models assuming continuous density distributions, namely that the relative emission from hot dust increases with decreasing viewing angle (see, e.g., Pier & Krolik 1992, their Figs. 4 and 5), is in general not observed for our sample.

Secondly, it appears that at any viewing angle the SEDs can have widely different shapes. However, we find trends with orientation for the relative strengths of both the warm and cool dust components. These trends, which are illustrated in Figs. 3 and 4, respectively, suggest that as the viewing angle decreases the warm and cool dust emissions

relative to that of the hot component *increase*. This result is contrary to the expectations of smooth-density torus models (see, e.g., Pier & Krolik 1992, their Figs. 5 and 7). The source 3C 84 stands out in both Figs. 3 and 4 as having a relatively weak hot dust component.

With the help of Fig. 2 we can identify differences and similarities between sources. Of special interest are possible shortcomings in the fits for those five sources that have two upper limits at the long-wavelength end, namely, 3C 207, 4C +28.45, 4C +34.47, 3C 263, and S5 0615+820, and the poorly constrained source 3C 245. Firstly, we note that the values of the upper limits for the two sources 4C +34.47 and 3C 263 are relatively low and, although located at different rest-frame wavelengths, appear to sample a similar cool blackbody component. Therefore, they are unlikely to be far from the true values. Secondly, based on the similarity between the SEDs of the sources 3C 207, 4C +28.45 and S5 0615+820, and those of the sources III Zw 2, 3C 390.3, and 4C +34.47, respectively, the peak of the cool blackbody component of the former is unlikely to be overestimated by factors $\gtrsim 2$. Finally, judging from a comparison between the SEDs of the sources 3C 245 and 3C 47, whereas the peaks of their cool blackbody components appear similar, the peak of the warm blackbody component of the former could be overestimated by a factor of ~ 2.

4.1.2   The silicate features

A characteristic property of interstellar dust are the spectral features centered at 9.7 μm and 18 μm due to silicates. In AGN, these features are expected to be produced by the dusty torus. A pertinent problem inherent to the measurement of silicate features remains the correct placement of the continuum, which ultimately decides if they are seen in emission or in absorption. This task is still challenging because the available spectra rarely cover a wavelength region large enough to see a sizeable portion of the continuum around the features, which are relatively broad and often shifted in wavelength (see Fig. 1). The advantage of our data set, however, is that the IRAC and MIPS photometry considerably extend the wavelength range of the IRS spectrum, thus allowing us to detect the *overall* continuum. In particular, our data shows that the 'dip' in the SED blueward of ~ 10 μm observed in most sources, which could be interpreted as blueshifted silicate absorption, is in fact the result of a warm dust component that is relatively weak.

Based on the overall continuum, we detect silicate *emission* in all our sources. The only exception is the source 3C 245, for which we do not detect strong silicate emission and interpret the IRS spectrum as being dominated by the warm and cool dust components. We have measured the properties of both the 10 μm and 18 μm silicate emission features after subtracting from the IRS spectrum the overall continuum fitted in Section 4.1.1 and removing superimposed strong narrow emission lines. Our results are listed in Table 7. We detect the 18 μm silicate feature in 4/8 sources, for which the IRS spectrum covers its location. In the remaining four sources this feature appears to be swamped by the cool blackbody component, which, based on its temperature (~ 200 K), peaks around this wavelength.

Our first noteworthy finding is that the 10 μm silicate emission feature is considerably redshifted in all our

Table 7. Properties of the Silicate Emission Features

Object Name[*]	θ	Silicate 10 μm				Silicate 18 μm			
		flux [erg/s/cm^2]	luminosity [erg/s]	W_λ [μm]	center [μm]	flux [erg/s/cm^2]	luminosity [erg/s]	W_λ [μm]	center [μm]
(1)	(2)	(3)	(4)	(5)	(6)	(7)	(8)	(9)	(10)
3C 207	8	4.42e−14	8.91e+43	0.65	10.31	–	–	–	–
3C 47	18	2.87e−13	1.86e+44	1.30	10.65	?	?	?	?
3C 336	23	8.45e−15	3.63e+43	0.37	10.13	–	–	–	–
4C +28.45	24	1.30e−13	1.91e+44	1.34	10.61	?	?	?	?
III Zw 2	28	2.38e−13	4.79e+42	0.16	10.53	?	?	?	?
4C +34.47	30	4.66e−13	5.75e+43	0.93	10.44	>1.04e−13	>1.29e+43	>0.29	?
3C 84	31	6.83e−12	5.01e+42	0.47	10.83	1.02e−11	7.41e+42	0.61	16.95
3C 334	34	7.94e−14	9.77e+43	0.43	10.53	–	–	–	–
3C 263	48	1.05e−13	1.86e+44	0.56	10.92	4.31e−14	7.76e+43	0.34	17.64
3C 390.3[†]	48	1.22e−12	9.12e+42	0.59	10.37	4.13e−13	3.09e+42	0.27	18.39
S5 0615+820	49	>1.11e−14	>2.51e+43	>0.42	>10.61	?	?	?	?

The columns are: (1) object name; (2) jet viewing angle; for the 10 μm silicate emission feature (3) integrated flux, (4) luminosity, (5) rest-frame equivalent width, and (6) rest-frame center of the emission; for the 18 μm silicate emission feature (7) integrated flux, (8) luminosity, (9) rest-frame equivalent width and (10) rest-frame center of the emission. A question mark indicates that the feature is not covered by the spectrum.

[*] objects presented in order of increasing jet viewing angle
[†] continuum fit used the IRAC data scaled to the IRS spectrum

sources. Instead of at the expected rest-frame wavelength of $\sim$ 9.7 μm, we find its center to lie in the range of $\sim$ $10.1 - 10.9$ μm (Table 7, column (6)). We note that strongly redshifted silicate emission features were observed previously in a few quasars (Siebenmorgen et al. 2005; Hao et al. 2005; Schweitzer et al. 2008), but never consistently in an entire sample. On the other hand, the center of the 18 μm silicate emission feature in the three objects for which it can be determined is strongly shifted in only one source (3C 84) and in this case blueward.

From circumstellar dust studies we know that the exact wavelength location of the silicate emission maximum depends on the grain size and composition, with larger grain sizes and larger amounts of crystalline dust (over amorphous dust) expected to enhance the emissivity at longer wavelengths (e.g., Bouwman et al. 2001). In order to investigate if this assumption holds also for AGN, we have plotted in Fig. 5 the luminosity of the 10 μm silicate feature versus its rest-frame center. Indeed, we find that stronger silicate emission is associated with a stronger redward displacement. However, the two lowest-luminosity sources (III Zw 2 and 3C 84) do not appear to follow this trend.

We note that in the current literature authors often study the (emission) equivalent widths of the silicate features rather than their luminosities. This approach needs to be taken with caution, since, by definition, the equivalent width depends strongly on the continuum flux. And, as the SEDs in Fig. 1 show, the 10 μm silicate feature is located such that its continuum flux is given by the relative strengths of the warm and cool blackbody components, which vary strongly between sources. In fact, the relation observed in Fig. 5 is not evident if we use rest-frame equivalent width values instead of luminosities, and our sample shows a trend for higher equivalent widths to be measured, the weaker the warm blackbody component is relative to the cool one.
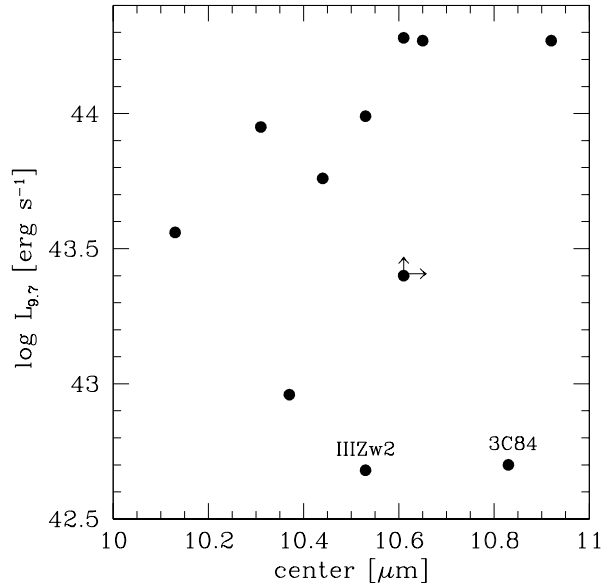

Figure 5. The luminosity of the 10 μm silicate emission feature versus the feature center. Arrows indicate limits.

4.1.3 The jet emission

We have selected our sample of radio-loud AGN based on their relatively large jet viewing angles ($\theta \gtrsim 20°$). At these orientations the relativistic enhancement of the jet emission is expected to be very low, ensuring that the observed infrared SED is dominated by emission from the putative dusty torus. In fact, based on the calculated relativistic Doppler factors δ (Table 1, column (16)), we expect relativistic beaming of the integrated jet flux, which is proportional to δ^4, by factors of $\lesssim 10$ in three sources (III Zw 2, 3C 84, and 3C 245) and relativistic *debeaming* for the remainder.
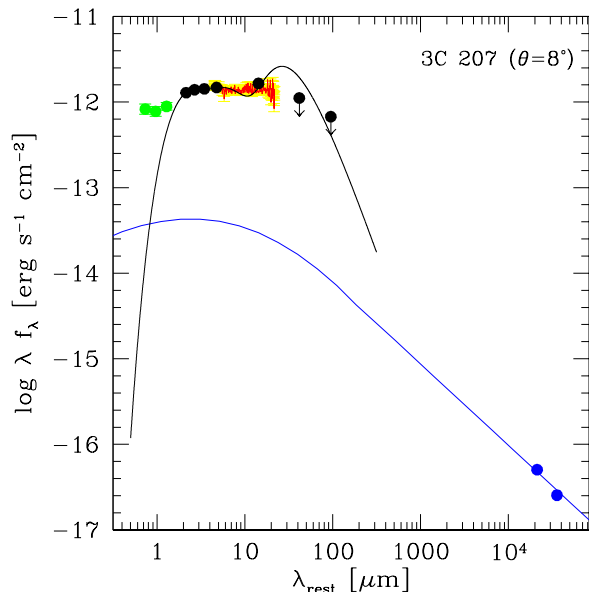
Figure 6. Infrared spectral energy distribution for 3C 207 from Fig. 1 extended to radio frequencies. An extrapolation of the radio core spectrum [8 GHz VLBI data (Hough et al. 2002) and 5 GHz VLA data (Hardcastle et al. 2004); blue filled circles] to higher frequencies using a typical blazar SED (blue solid curve) shows that even in our strongest relativistically beamed source the jet does not dominate the infrared emission.
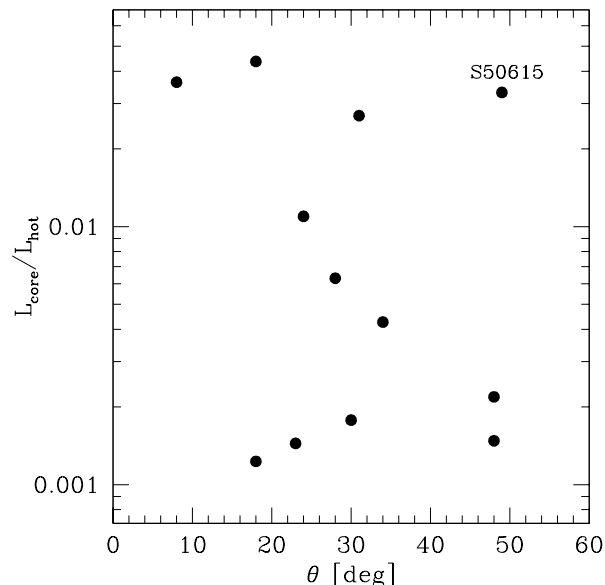

Figure 7. The ratio between the integrated core radio luminosity and the peak luminosity of the hot blackbody component versus the jet viewing angle.

The exception is the source 3C 207, for which, based on improved proper motion data, we now calculate a relatively small inclination angle ($\theta \sim 8°$). Its relativistic Doppler factor is $\delta \sim 3$, meaning that the relativistic jet flux enhancement is expected to be a factor of ~ 80. However, as Fig. 6 shows, even in the strongest relativistically beamed source

in our sample the infrared SED is dominated by thermal emission. An extrapolation of the core radio spectrum using a typical blazar SED that generally peaks at a few μm (Giommi et al. 2002) predicts mid-infrared fluxes a factor of ~ 40 lower than observed.

Further evidence that the infrared SEDs of all our sources are dominated by thermal rather than non-thermal emission comes from their similar, relatively bulgy appearance and the lack of strong, short-term variability. The IRS spectroscopy overlaps in wavelength with either the IRAC and/or the MIPS photometry, and an impressive consistency is evident between the two data sets, which were taken several months apart (see Tables 2 and 3). Variability is detected in the source 3C 390.3, however, not of the strength typical of blazars. The flux increase is a factor of < 2 over a period of four years.

Given that the infrared emission in our sources is thermal and that the hot dust emission seems to be emitted isotropically (see Section 4.1.1), we can now carry out a consistency check for the calculated viewing angles. Along the lines of argument presented by Wills & Brotherton (1995), we plot in Fig. 7 the ratio between the integrated core radio luminosity (calculated from the data listed in Table 1) and the peak luminosity of the hot blackbody component (calculated from the fluxes listed in Table 6, column (7)) versus the jet viewing angle. In such a diagram, we expect that the stronger a source is relativistically beamed, the higher its ratio between beamed and isotropic emission. Fig. 7 shows that the resulting trend in viewing angle for our sample is qualitatively correct; the smaller the viewing angle, the higher the ratio between (beamed) core radio power and (isotropic) dust luminosity. The only pronounced exception is the source S5 0615+820, for which the viewing angle appears to be highly overestimated.

4.2 Testing CLUMPY torus models

Due to the shortcomings in AGN torus models invoking continuous dust distributions, new models based on clumpy media have recently been put forward (e.g., Schartmann et al. 2005, 2008; Hönig et al. 2006; Hönig & Kishimoto 2010; Nenkova et al. 2002, 2008a,b). The most detailed of these models are those of Nenkova and collaborators (named CLUMPY), and they can be accessed on-line[2]. In short, these authors solved the radiative transfer problem in clumpy media by assuming that the medium is composed of clouds that are individually optically thick ($\tau_V \gg 1$), that each cloud can be considered a point source of intensity $S_{c,\lambda}$, and that the cloud distribution obeys Poisson statistics. In this case, the escape probability of the emitted radiation can be approximated as $P_{esc} \simeq e^{-N_T}$, with N_T the total number of clouds along the line of sight, and the intensity at a given location becomes:

$$I_\lambda^C(s) = \int^s e^{-N_T(s,s')} S_{c,\lambda} N_C(s') ds', \qquad (3)$$

where N_C is the radial cloud density (i.e., the number of clouds per unit length). With this formalism the only difference between the clumpy and continuous cases is that
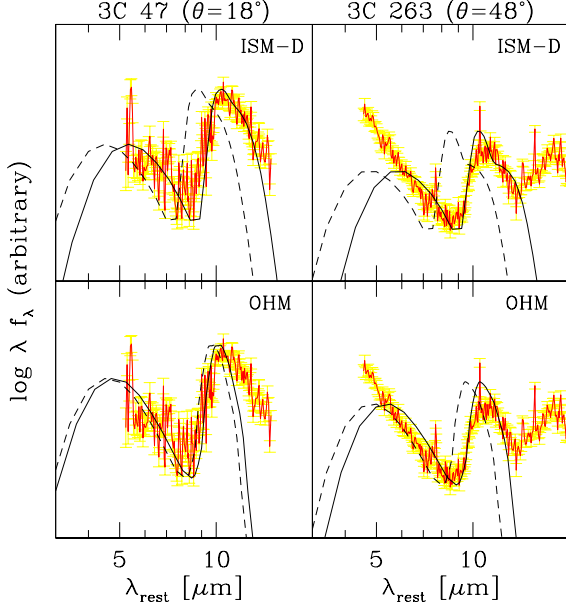

Figure 8. The 10 μm silicate emission feature and the spectral slope blueward of it are well approximated by *redshifted* CLUMPY models with standard ISM dust composition (code ISM-D; top panels, solid lines). Dust composed of silicates with various materials added (code OHM; bottom panels) does not reproduce the observations as well, independent of whether we apply a redshift (solid lines) or not (dashed lines).

Figure 9. The height of the 10 μm silicate emission peak relative to the 'dip' blueward of it constrains best the number of clouds (top panels, where dotted, solid and dashed lines indicate $N_0 = 4$, 5 and 6, respectively), the power-law index of the radial cloud distribution (middle panels, where dotted, solid and dashed lines indicate $q = 1$, 2 and 3, respectively), and the angular width of the Gaussian cloud distribution (bottom panels, where dotted, solid and dashed lines indicate $\sigma = 30°$, $45°$ and $60°$, respectively).

optical depth τ_V is replaced by its effective equivalent $N_T(1 - e^{-\tau_V}) \simeq N_T$ (for $\tau_V \gg 1$) and the absorption coefficient is replaced by N_C. The main challenge lies with the calculation of the clump source function, $S_{c,\lambda}$, that needs to properly take into account the illumination profile of the individual clouds and the effects of cloud shadowing.

In this section we wish to test the CLUMPY models, in particular how well they approximate the entire infrared SED, how unique a fitting set of parameters is and what physics can be extracted. For simplicity, we will limit ourselves to models invoking a torus geometry with a Gaussian angular cloud distribution, i.e., we will not consider a spherical distribution or the sharp-edge geometry.

4.2.1 Constraining the parameters

The CLUMPY torus models are available for two different dust compositions and have six parameters that can be adjusted: the optical depth of the cloud, τ_V, the average number of clouds along an equatorial line of sight, N_0, the power-law index of the radial cloud distribution, q, the angular width of the Gaussian cloud distribution, σ, the ratio between the outer and inner torus radius, Y, and the viewing angle, θ. The dust composition is assumed to be a mix of silicates and graphite with silicates either as in the standard interstellar medium (Draine 2003, code ISM-D) or with various materials added (Ossenkopf et al. 1992, code OHM).

In general, the problem that one faces when choosing a CLUMPY model that best-fits the data is that its parameters are highly degenerate, with several permutations yielding very similar results (Asensio Ramos & Ramos Almeida
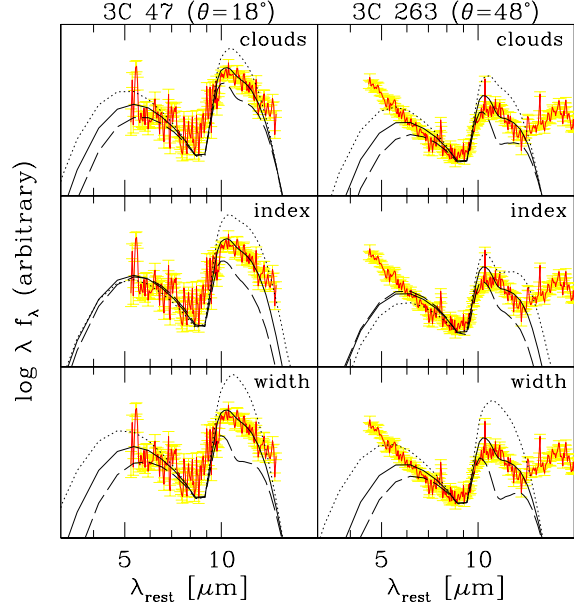
2009; Ramos Almeida et al. 2009; Nikutta et al. 2009). In the following, we introduce an effective method to select a suitable model (by eye) and find that the high degeneracy is due to the fact that, with the exception of the dust composition, all parameters constrain only the radial mass density profile (and so the radial temperature profile). This then means that, although CLUMPY cannot uniquely determine the AGN torus structure, it is a versatile tool with possible application to other astrophysical objects.

As a first step, we find that our observations can constrain the dust composition. As Fig. 8 shows, ISM-D models approximate well both the shape of the 10 μm silicate emission feature and the spectral slope blueward of it, however, only if a redshift is applied (top panels). On the other hand, OHM models predict a narrower silicate feature than is observed and do not match well the blueward spectral flux, independent of whether we apply a redshift or not (bottom panels). We have then used in the following only ISM-D models. In this respect, we note that our result differs from, but does not contradict, that of Sirocky et al. (2008). These authors constrain the dust composition of ultraluminous infrared galaxies based on the strengths of both the 10 μm and 18 μm silicate features to be that of the OHM models. However, a careful inspection of their Figs. 7-9 shows that their method cannot constrain the dust composition in type-1 AGN, such as our sources.

Next, we find that the most convenient and reliable way to constrain the five geometrical CLUMPY parameters is to use the height of the 10 μm silicate emission peak relative to the 'dip' blueward of it. Then, this flux ratio is larger, the smaller N_0, q, σ and θ, and the larger Y are. The most

Table 8. CLUMPY Torus Model Fit Results

Object Name[*]	θ [deg]	z_C	τ_V	N_0	q	L_{bol} [erg/s]	R_{in} [pc]	M_C [$M_\odot$]
(1)	(2)	(3)	(4)	(5)	(6)	(7)	(8)	(9)
3C 207	8	0.225	10	7	3	1.12e+46	1.340	8.5e+04
3C 47	18	0.186	10	5	2	1.15e+46	1.355	1.3e+05
3C 245	18	0.225	150	20	3	3.47e+46	2.355	1.1e+07
3C 336	23	0.202	10	5	3	9.77e+45	1.250	5.3e+04
4C +28.45	24	0.167	10	4	2	1.41e+46	1.503	1.3e+05
III Zw 2	28	0.230	10	7	3	1.48e+45	0.486	1.1e+04
4C +34.47	30	0.186	10	5	2	4.07e+45	0.807	4.7e+04
3C 84	31	0.109	150	20	3	3.09e+44	0.222	1.0e+05
3C 334	34	0.067	150	20	3	9.33e+45	1.222	3.0e+06
3C 263	48	0.230	10	5	2	3.55e+46	2.383	4.1e+05
3C 390.3	48	0.175	10	5	1	9.55e+44	0.391	2.4e+04
S5 0615+820	49	0.202	10	4	1	6.61e+45	1.028	1.3e+05

The columns are: (1) object name; (2) jet viewing angle; for the CLUMPY component: (3) redshift, (4) cloud optical depth, (5) number of clouds along equatorial rays, (6) power-law index of the radial cloud distribution, (7) bolometric luminosity, (8) inner radius, and (9) mass in clouds (in solar masses). In all cases we assumed parameters $\sigma = 45$ and $Y = 10$.

[*] objects presented in order of increasing jet viewing angle

pronounced differences are produced by changing N_0, q, and σ (Fig. 9), and the strongest degeneracy seems to be present between N_0 and θ (i.e., we obtain a similar result, if we either increase N_0 and decrease θ or vice versa). Since all these parameters effectively determine the cloud number density (see eq. (2) of Nenkova et al. (2008b)), and the aforementioned degeneracy serves to keep it constant, this then means that our flux ratio is larger, the smaller N_C. Once N_C is fixed, the selection of τ_V is straightforward, since models with small values predict much stronger 10 μm silicate emission and much less radiation at far-IR wavelengths than models with large values (see Fig. 5 of Nenkova et al. 2008b).

4.2.2 Revealing the strengths and deficits

Applying the CLUMPY models to the infrared SEDs of our sources, we find in all cases that they can approximate well the mid-IR part, but significantly underpredict the flux at both near-IR and far-IR wavelengths. Furthermore, it is always necessary to apply a redshift to the models. We show the models (including the predicted AGN contribution) in Fig. 10 (black solid curves) and list the fitting set of parameters in Table 8.

The cold dust component unaccounted for by CLUMPY models is ubiquitously observed in AGN and has been associated with dust from either starbursts and/or the narrow emission line region (NELR) (e.g., Netzer et al. 2007; Schweitzer et al. 2008; Mor et al. 2009). The first alternative is unlikely to hold for our sample for three reasons: (i) radio-loud AGN reside predominantly in luminous ellipticals, which usually do not have significant starbursts; (ii) we do not observe strong polycyclic aromatic hydrocarbon (PAH) features in our IRS spectra, which are usually associated with starbursts; and (iii) the observed peak luminosities of the cold dust components are of the order of $L_{cold} \sim 10^{10} - 10^{12}$ solar luminosities, implying that the starburts would have to be unusually luminous. On the other

hand, models for the dust emission from the NELR usually predict higher temperatures and, therefore, aim to account mainly for the wavelength region covered by CLUMPY models (Mor et al. 2009).

Besides the cold dust component, CLUMPY cannot account for the hottest dust. The reason for this might be simply that its chemical composition differs from that assumed by the models. For example, it could be composed of pure graphite, which has a higher sublimation temperature than silicates and emits a spectrum close to a pure blackbody. Other authors have previously hinted at such an origin for the hot dust component (e.g., Mor et al. 2009).

The redshifts required to displace the models are relatively large ($z_C \sim 0.07 - 0.23$). Fig. 11 shows these redshifts compared to those we derive from the measured center of the 10 μm silicate emission feature (Table 7), with the latter redshifts calculated assuming the peak rest-frame wavelength of the ISM-D silicates (9.5 μm instead of 9.7 μm). With the exception of the two sources that are modeled with a very high optical depth (3C 84 and 3C 334, see below), which makes the determination of z_C rather uncertain, the CLUMPY redshifts are always larger. In order to understand this finding we recall that we determine z_C by adjusting the CLUMPY model to the location of the 'dip' blueward of the silicate feature and thus to the feature's blue wing, whereas the measurement of the emission center depends strongly on the width of the feature's top part. However, as CLUMPY shows (Fig. 12), the width of the top part is reduced as the cloud number density and so the absorption increases, which leads to an apparent blueshift of the emission peak and thus an underestimating of the (true) redshift. This radiative transfer effect then also offers an alternative explanation for the relation found in Fig. 5. Instead of a difference in grain size, it could be that the larger the observed redshift of the center, the less absorbed the silicate feature is, and so the larger its luminosity (for
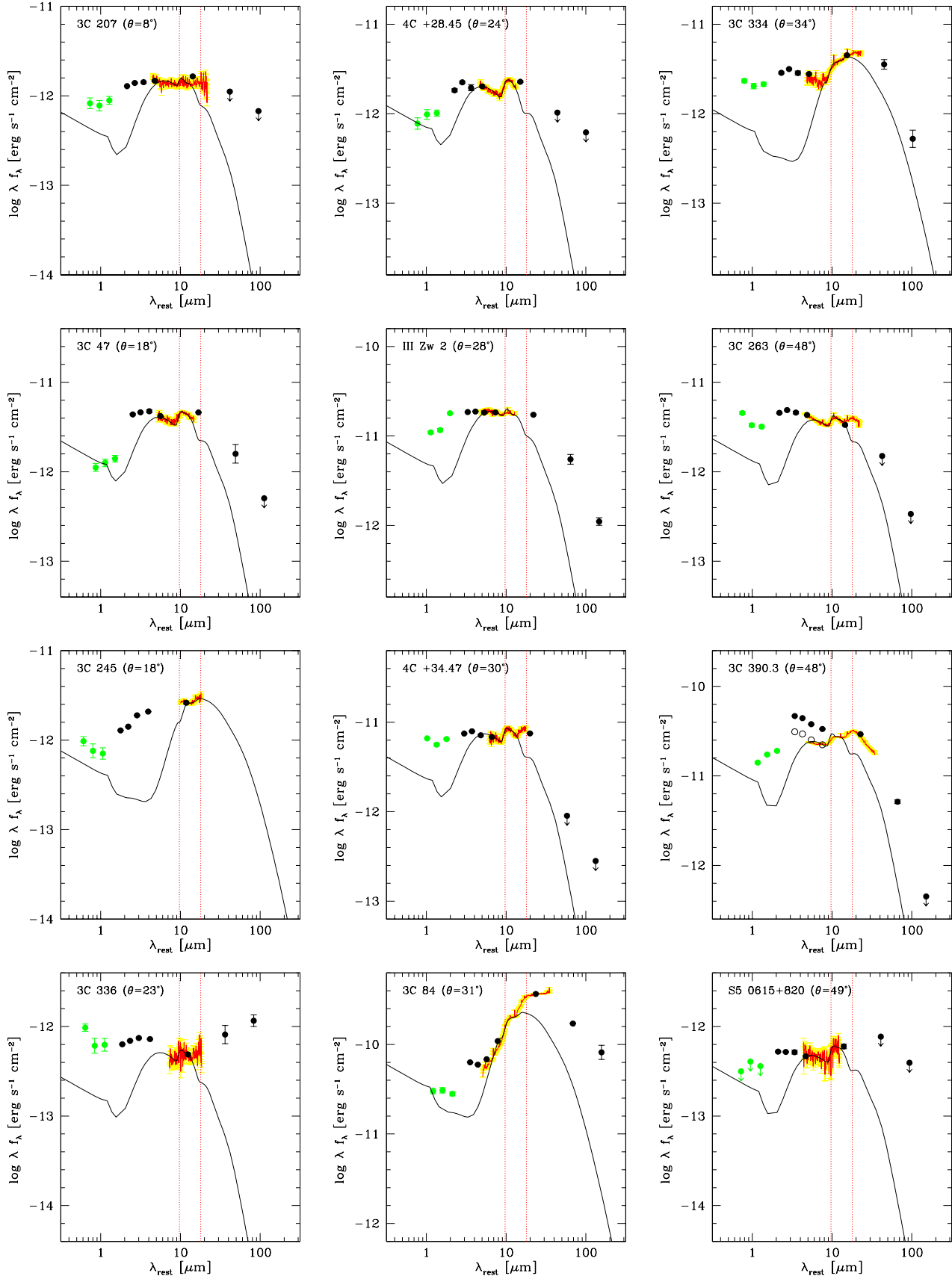
Figure 10. Infrared spectral energy distributions from Fig. 1 with *redshifted* CLUMPY torus models overlaid (solid black curves).

the same AGN bolometric luminosity, as is the case for our sample; see below).

Recently, Nikutta et al. (2009) proposed that the observed redshifts of the 10 μm silicate emission features in AGN can be explained by an interplay between the radiative transfer effects illustrated in Fig. 12 and a rising continuum underneath the feature. In particular, they showed that the appearance of the feature's top part can change from less to more peaked depending on if the region between the 10 μm and 18 μm silicate features was included in the continuum fit or not. In this respect we note that we have included the middle continuum part in our fit and have measured the center (not the peak) of the feature, which is less sensitive to the continuum placement. Furthermore, as Fig. 12 shows, the radiative transfer effects mentioned by Nikutta et al. (2009) *decrease* the observed redshifts and so cannot explain them (see also Hönig et al. 2010).

The large majority of our sources are best modelled assuming a cloud optical depth of $\tau_V = 10$, with only three objects (3C 245, 3C 84, and 3C 334) requiring a much larger value of $\tau_V = 150$ in order to produce enough emission at large ($\lambda \gtrsim 20\ \mu$m) wavelengths. The number of clouds along equatorial rays and the index of the radial cloud distribution differ the most among our sources, with required values of $N_0 = 4, 5, 7$ and 20, and $q = 1, 2$ and 3, respectively. On the other hand, we find that it is not necessary to vary the ratio between the outer and inner torus radius and the width of the Gaussian distribution, with values of $Y = 10$ and $\sigma = 45°$, respectively, giving satisfactory results.

Several physical parameters can be derived from an approximation of the infrared SED with CLUMPY models. The most important of these are the bolometric luminosity of the source, the inner radius of the CLUMPY component, and the observed mass in clouds (Table 8). The bolometric luminosity can be readily obtained from the scaling of the model to the data, taking into account that the model is redshifted and thus the observed flux reduced by a factor of $(1 + z_C)^2$. The resulting values for our sources span only ~ 2 orders of magnitude and we note that in particular the nine objects that follow a relation in Fig. 5 have similar values ($\langle \log L_{\mathrm{bol}} \rangle = 45.9 \pm 0.1$ erg s^{-1}). Using the bolometric luminosity and eq. (1) of Nenkova et al. (2008b) we have then calculated the inner radius of the CLUMPY component, R_{in}, assuming a dust sublimation temperature of $T_{\mathrm{sub}} = 1500$ K. We obtain values in the range of $R_{\mathrm{in}} \sim 0.2 - 2$ pc.

The calculation of the total mass in clouds follows eq. (6) of Nenkova et al. (2008a) and relies on the cloud number density, N_C. Nenkova et al. (2008b) give an analytic expression for the mass in the case of the sharp-edge geometry that differs only slightly from the proper numerical integration in the case of a Gaussian toroidal geometry:

$$M_C = m_H N_H \int N_C \, dV = m_H \frac{\tau_V}{\sigma_V} R_{\mathrm{in}}^2 N_0 I_q 4\pi \sin \sigma, \qquad (4)$$

where m_H is the proton mass, N_H is the hydrogen column density of a cloud, σ_V=4.89e−22 cm^2 (Draine 2003) is the dust absorption cross-section in the V band, and $I_q = (Y^2 - 1)/(2\ln Y)$, Y, and $(2\ln Y)/(1 - Y^{-2})$ for the case of $q = 1, 2$, and 3, respectively. Since the degeneracy inherent to CLUMPY serves to keep the mass density constant, the determination of M_C is expected to be robust, i.e.,
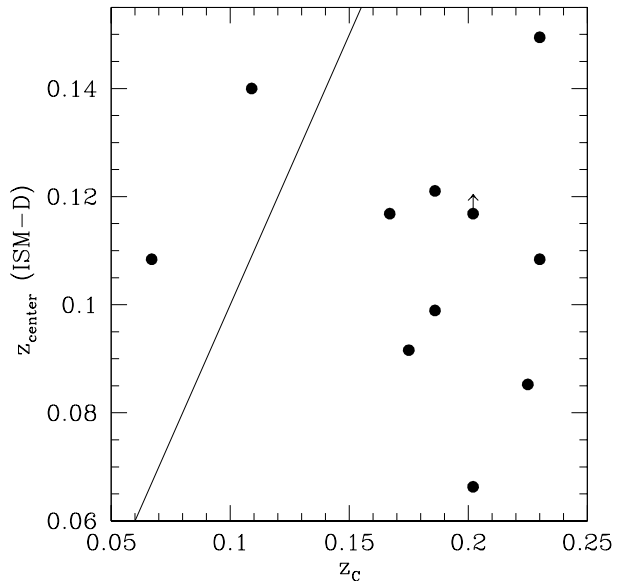

Figure 11. The redshift of the center of the 10 μm silicate emission feature versus the redshift required to displace the CLUMPY models. The solid line marks the locus of equality. Arrows indicate limits.
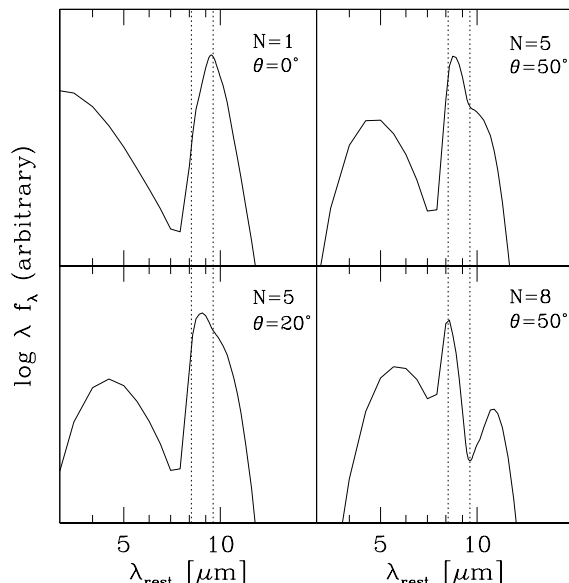

Figure 12. The emission peak of the 10 μm silicate feature appears increasingly blueshifted as self-absorption becomes important. In the examples shown the feature center has shifted from 9.5 μm (top left panel) to 8.1 μm (bottom right panel) (vertical dotted lines).

one should get the same result with any fitting set of model parameters.

5   SUMMARY AND CONCLUSIONS

We have presented infrared observations obtained with all three instruments on-board the *Spitzer Space Telescope* for 12 radio-loud AGN, for which actual viewing angles can be determined. The results of our analysis of the infrared SED and the strength of the 10 μm silicate feature can be summarized as follows:

1. The infrared SED is best-fit with a combination of three or four blackbodies. The resulting temperatures for the hot, warm, cool and cold components are in the ranges $T_{\rm hot} \sim 1200-2000$ K, $T_{\rm warm} \sim 300-800$ K, $T_{\rm cool} \sim 150-250$ K, and $T_{\rm cold} \sim 60-150$ K, respectively.

2. We find trends between the emissions of the warm and cool dust components and the jet viewing angle indicating that the more the source is viewed face-on, the *larger* the amount of dust that comes into our line of sight. No such trend is present for the hot dust component. Both these results are contrary to the expectations of smooth-density torus models.

3. Based on the overall continuum, we detect the 10 μm silicate feature in *emission* in all our sources. The feature center is always observed to be strongly redshifted.

4. We test the CLUMPY torus models of Nenkova and collaborators and find that they approximate well the mid-infrared part of the SED, but significantly underpredict the fluxes at both near-IR and far-IR wavelengths. Furthermore, we find that the models can constrain the dust composition (in our case to that of the standard ISM), that they require relatively large redward displacements ($\sim 10\% - 20\%$ the speed of light) to match the observations, and that they are insensitive to the assumed geometry but give robust total mass estimates.

REFERENCES

Antonucci, R. 1993, ARA&A, 31, 473

Antonucci, R., & Miller, J. S. 1985, ApJ, 297, 621

Asensio Ramos, A., & Ramos Almeida, C. 2009, ApJ, 696, 2075

Bouwman, J., Meeus, G., de Koter, A., Hony, S., Dominik, C., & Waters, L. B. F. M. 2001, A&A, 375, 950

Brinkmann, W., Yuan, W., & Siebert, J. 1997, A&A, 319, 413

Brunthaler, A., Falcke, H., Bower, G. C., Aller, M. F., Aller, H. D., & Teräsranta, H. 2005, A&A, 435, 497

Buchanan, C. L., Gallimore, J. F., O'Dea, C. P., Baum, S. A., Axon, D. J., Robinson, A., Elitzur, M., & Elvis, M. 2006, AJ, 132, 401

Carpenter, J. M., et al. 2008, ApJS, 179, 423

Clavel, J., et al. 2000, A&A, 357, 839

Cleary, K., Lawrence, C. R., Marshall, J. A., Hao, L., & Meier, D. 2007, ApJ, 660, 117

Cohen, M. H., Ogle, P. M., Tran, H. D., Goodrich, R. W., & Miller, J. S. 1999, AJ, 118, 1963

Draine, B. T. 2003, ARA&A, 41, 241

Efstathiou, A., & Rowan-Robinson, M. 1995, MNRAS, 273, 649

Engelbracht, C. W., et al. 2007, PASP, 119, 994

Evans, D. A., Worrall, D. M., Hardcastle, M. J., Kraft, R. P., & Birkinshaw, M. 2006, ApJ, 642, 96

Fazio, G. G., et al. 2004, ApJS, 154, 10

Fey, A. L., & Charlot, P. 2000, ApJS, 128, 17

Gambill, J. K., Sambruna, R. M., Chartas, G., Cheung, C. C., Maraschi, L., Tavecchio, F., Urry, C. M., & Pesce, J. E. 2003, A&A, 401, 505

Ghisellini, G., Padovani, P., Celotti, A., & Maraschi, L. 1993, ApJ, 407, 65

Giommi, P., Capalbi, M., Fiocchi, M., Memola, E., Perri, M., Piranomonte, S., Rebecchi, S., & Massaro, E. 2002, in Blazar Astrophysics with BeppoSAX and Other Observatories, ed. P. Giommi, E. Massaro, & G. Palumbo (ASI/ESA), 63

Gordon, K. D., et al. 2007, PASP, 119, 1019

Granato, G. L., & Danese, L. 1994, MNRAS, 268, 235

Haas, M., Siebenmorgen, R., Schulz, B., Krügel, E., & Chini, R. 2005, A&A, 442, L39

Hao, L., et al. 2005, ApJ, 625, L75

Hao, L., Weedman, D. W., Spoon, H. W. W., Marshall, J. A., Levenson, N. A., Elitzur, M., & Houck, J. R. 2007, ApJ, 655, L77

Hardcastle, M. J., Birkinshaw, M., Cameron, R. A., Harris, D. E., Looney, L. W., & Worrall, D. M. 2002, ApJ, 581, 948

Hardcastle, M. J., Evans, D. A., & Croston, J. H. 2006, MNRAS, 370, 1893

Hardcastle, M. J., Harris, D. E., Worrall, D. M., & Birkinshaw, M. 2004, ApJ, 612, 729

Hardcastle, M. J., & Worrall, D. M. 1999, MNRAS, 309, 969

Higdon, S. J. U., et al. 2004, PASP, 116, 975

Hiner, K. D., Canalizo, G., Lacy, M., Sajina, A., Armus, L., Ridgway, S., & Storrie-Lombardi, L. 2009, ApJ, 706, 508

Hönig, S. F., Beckert, T., Ohnaka, K., & Weigelt, G. 2006, A&A, 452, 459

Hönig, S. F., & Kishimoto, M. 2010, A&A, arXiv:0909.4539

Hönig, S. F., Kishimoto, M., Gandhi, P., Smette, A., Asmus, D., Duschl, W., Polletta, M., & Weigelt, G. 2010, A&A, arXiv:1003.0920

Hooimeyer, J. R. A., Barthel, P. D., Schilizzi, R. T., & Miley, G. K. 1992a, A&A, 261, 1

Hooimeyer, J. R. A., Schilizzi, R. T., Miley, G. K., & Barthel, P. D. 1992b, A&A, 261, 5

Houck, J. R., et al. 2004, ApJS, 154, 18

Hough, D. H., & Readhead, A. C. S. 1987, ApJ, 321, L11

Hough, D. H., Readhead, A. C. S., Wood, D. A., Jr., & Feldmeier, J. J. 1992, ApJ, 393, 81

Hough, D. H., Vermeulen, R. C., Readhead, A. C. S., Cross,

L. L., Barth, E. L., Yu, L. H., Beyer, P. J., & Phifer, E. M. 2002, AJ, 123, 1258

Kellermann, K. I., et al. 2004, ApJ, 609, 539

Krolik, J. H. 2007, ApJ, 661, 52

Krolik, J. H., & Begelman, M. C. 1988, ApJ, 329, 702

Lawrence, A. 1987, PASP, 99, 309

Linfield, R. 1981, ApJ, 244, 436

Lister, M. L., et al. 2009, AJ, 137, 3718

Lumsden, S. L., Heisler, C. A., Bailey, J. A., Hough, J. H., & Young, S. 2001, MNRAS, 327, 459

Makovoz, D., & Marleau, F. R. 2005, PASP, 117, 1113

Markwardt, C. B. 2009, in Astronomical Data Analysis Software and Systems XVIII, ed. D. Bohlender, P. Dowler, & D. Durand, ASP Conference Series, arXiv:0902.2850v1

Marscher, A. P. 1987, in Superluminal Radio Sources, ed. J. A. Zensus & T. J. Pearson, 280

Mor, R., Netzer, H., & Elitzur, M. 2009, ApJ, 705, 298

Nenkova, M., Ivezić, Z., & Elitzur, M. 2002, ApJ, 570, L9

Nenkova, M., Sirocky, M. M., Ivezić, Z., & Elitzur, M. 2008a, ApJ, 685, 147

Nenkova, M., Sirocky, M. M., Nikutta, R., Ivezić, Z., & Elitzur, M. 2008b, ApJ, 685, 160

Netzer, H., et al. 2007, ApJ, 666, 806

Nikutta, R., Elitzur, M., & Lacy, M. 2009, ApJ, 707, 1550

Ogle, P., Whysong, D., & Antonucci, R. 2006, ApJ, 647, 161

Ossenkopf, V., Henning, T., & Mathis, J. S. 1992, A&A, 261, 567

Page, K. L., Schartel, N., Turner, M. J. L., & O'Brien, P. T. 2004, MNRAS, 352, 523

Piconcelli, E., Jimenez-Bailón, E., Guainazzi, M., Schartel, N., Rodríguez-Pascual, P. M., & Santos-Lleó, M. 2005, A&A, 432, 15

Pier, E. A., & Krolik, J. H. 1992, ApJ, 401, 99

Pier, E. A., & Krolik, J. H. 1993, ApJ, 418, 673

Prieto, M. A. 1996, MNRAS, 282, 421

Ramos Almeida, C., et al. 2009, ApJ, 702, 1127

Reach, W. T., et al. 2005, PASP, 117, 978

Readhead, A. C. S., Hough, D. H., Ewing, M. S., Walker, R. C., & Romney, J. D. 1983, ApJ, 265, 107

Rieke, G. H., et al. 2004, ApJS, 154, 25

Roche, P. F., Aitken, D. K., Smith, C. H., & Ward, M. J. 1991, MNRAS, 248, 606

Rokaki, E., Lawrence, A., Economou, F., & Mastichiadis, A. 2003, MNRAS, 340, 1298

Salpeter, E. E. 1977, ARA&A, 15, 267

Sambruna, R. M. 1997, ApJ, 487, 536

Schartmann, M., Meisenheimer, K., Camenzind, M., Wolf, S., & Henning, T. 2005, A&A, 437, 861

Schartmann, M., Meisenheimer, K., Camenzind, M., Wolf, S., Tristram, K. R. W., & Henning, T. 2008, A&A, 482, 67

Schweitzer, M., et al. 2008, ApJ, 679, 101

Shi, J., & Krolik, J. H. 2008, ApJ, 679, 1018

Shi, Y., et al. 2006, ApJ, 653, 127

Siebenmorgen, R., Haas, M., Krügel, E., & Schulz, B. 2005, A&A, 436, L5

Sirocky, M. M., Levenson, N. A., Elitzur, M., Spoon, H. W. W., & Armus, L. 2008, ApJ, 678, 729

Skrutskie, M. F., et al. 2006, AJ, 131, 1163

Spoon, H. W. W., Keane, J. V., Tielens, A. G. G. M., Lutz, D., Moorwood, A. F. M., & Laurent, O. 2002, A&A, 385, 1022

Stansberry, J. A., et al. 2007, PASP, 119, 1038

Thompson, G. D., Levenson, N. A., Uddin, S. A., & Sirocky, M. M. 2009, ApJ, 697, 182

Tristram, K. R. W., et al. 2007, A&A, 474, 837

Tristram, K. R. W., et al. 2009, A&A, 502, 67

Urry, C. M., & Padovani, P. 1995, PASP, 107, 803

van Bemmel, I. M., & Dullemond, C. P. 2003, A&A, 404, 1

Vermeulen, R. C., & Cohen, M. H. 1994, ApJ, 430, 467

Weedman, D. W., et al. 2005, ApJ, 633, 706

Wills, B. J., & Brotherton, M. S. 1995, ApJ, 448, L81